Ceramics International 50 (2024) 20843–20850

Contents lists available at ScienceDirect

Ceramics International

journal homepage: www.elsevier.com/locate/ceramint

Design of a new ZnO photocatalytic Fenton-like system for enhancing the removal of methylene blue at neutral pH

Elie A. Daher [a,b], Abbass Al Redda [a], Christel Laberty Robert [b,c], Wael Hamd [d,*]

[a] Petrochemical Engineering Department, Faculty of Engineering III, CRSI, Lebanese University, Rafic Hariri Campus, Hadat, Lebanon
[b] Laboratoire Chimie de la Matière Condensée de Paris LCMCP, Sorbonne Université, UPMC Paris 06, 4 Place Jussieu, 75005, Paris, France
[c] RS2E, Réseau Français sur le Stockage Electrochimique de l'Energie, CNRS 3459, 80039 Cedex 1, Amiens, France
[d] Chemical Engineering Department, Faculty of Engineering, University of Balamand, P.O. Box 33, El-Koura, Lebanon

ARTICLE INFO

Handling Editor: Dr P. Vincenzini

Keywords:
ZnO thin films
Photocatalysis
Photo Fenton-like
Degradation rate
Pseudo-first-order

ABSTRACT

Although doping, nanostructuration, metallization, and binary/ternary oxide systems are widely used to improve the degradation kinetics in photocatalytic processes, rapid electron - hole recombination remains one of its major limitations. On the other hand, homogeneous photo-Fenton-like processes suffer from the slow regeneration of Fe^{3+}/Fe^{2+} catalysts and the formation of iron sludge at pH > 3. In this work, a new catalytic system is designed based on the coupling of nanostructured ZnO thin films photocatalysts with Fe^{3+}/H_2O_2 (Fenton-Like) for the degradation of methylene blue (MB) molecules under UVA irradiation, at near-neutral pH (7.5). This coupled process promotes the formation of additional reactive oxygen species and reduces the formation of sludge by accelerating the regeneration of the iron catalysts in the medium. Furthermore, it exhibits a single kinetic regime of degradation with a rate constant of 0.0049 min^{-1} exceeding the sum of both individual processes and allowing therefore the removal of 94 % of MB after 480 min.

1. Introduction

The low efficiency and high cost of conventional treatment techniques to tackle recalcitrant organic molecules in aqueous mediums have motivated the scientific community to develop alternative and innovative technologies [1]. In this scope advanced oxidation processes (AOPs) have gained significant attention during the last decade [2–5]. Amongst these AOPs, heterogeneous photocatalysis and Fenton processes have emerged as attractive and efficient methods [1,6–8]. For instance, photocatalysis is based on the generation of highly reactive oxygen species (ROS) such as hydroxyl radical ($OH^{\bullet}$) and superoxide radical ($O_2^{\bullet-}$) upon the exposure of a photocatalytic material to an irradiation source [9]. These ROS are well-known for their strong oxidation capacity toward organic matter, leading to their transformation into less hazardous molecules such as H_2O and CO_2 [10–13]. Amongst the photocatalysts, zinc oxide (ZnO) exhibits strong oxidation ability, low production price, and low degree of toxicity to marine/human life [14–17]. Nonetheless, the material photoactivity is hampered by the rapid recombination rate of the electron - hole pairs ($\bar{e}$- h^+) charge carrier [1, 14,18,19]. On the other hand, Fenton oxidation is considered an effective technique for the remediation of emerging contaminants in water and wastewater effluents due to the procedure's simplicity, usage of inexpensive reagents, and strong oxidation abilities [6,20–22]. Particularly, homogeneous photo-Fenton processes exhibit faster degradation rates compared to conventional Fenton due to the high amount of generated ($OH^{\bullet}$) via the reaction between Fe^{2+} and H_2O_2 [23]. However, the iron salt catalyst cannot be reused in additional cycles, due to its precipitation at pH > 3 in the form of iron sludge [6]. Thus, heterogeneous photo-Fenton processes were developed by replacing the Fe^{2+} ions with solid catalysts, then limiting the iron ions from leaching [24–26]. Despite the recent advances in Fenton processes [6,27], they are still suffering from the narrow working pH range, the use of chelating agents, and the formation of sludge, disfavoring then their usage on an industrial scale.

To overcome the limitations of both processes (photocatalysis and photo-Fenton), we designed in this work a new process that couples wrinkled ZnO photocatalyst with Fe^{3+}/H_2O_2 under UVA irradiation. This is designed for the degradation of methylene blue at near-neutral pH. With both processes running concurrently, a win-win situation is achieved, i.e. the photo-generated electrons by the photocatalyst are trapped by the iron (III), inhibiting electron - hole recombination from one side, and accelerating the Fe^{3+}/Fe^{2+} regeneration from the other

* Corresponding author.
E-mail address: wael.hamd@balamand.edu.lb (W. Hamd).

https://doi.org/10.1016/j.ceramint.2024.02.243
Received 27 October 2023; Received in revised form 4 February 2024; Accepted 19 February 2024
Available online 22 February 2024

side. This innovative system enhances the degradation kinetics of the organic pollutants due to the presence of high concentrations of ($OH^{\bullet}$), generated through the presence of "free iron ions" and the ZnO photocatalyst consequently (Rn 1 - 3) [27–29]:

$Fe^{3+} + H_2O_2 \rightarrow Fe^{2+} + H^+ + HO_2^{\bullet}$ (Fenton) (Rn.1)

$Fe^{2+} + H_2O_2 \rightarrow Fe^{3+} + OH^- + {}^{\bullet}OH$ (Fenton) (Rn.2)

$ZnO + hv \rightarrow O_2^{\bullet-} + {}^{\bullet}OH$ (Photocatalysis) (Rn.3)

2. Experimental section

2.1. Reagents and materials

97% analytical grade zinc acetate dihydrate ($Zn(CH_3COO)_2{\cdot}2H_2O$) was obtained from ACROS organics, propan-2-ol (analytical reagent grade) from Fisher Scientific, monoethanolamine (MEA) (98 % analytical grade) from Fisher Scientific, iron (III) nitrate nonahydrate ($Fe(NO_3)_3{\cdot}9\ H_2O$) 99% for analysis from ACROS Organics, Hydrogen peroxide (H_2O_2) solution 30% (w/w) from Riedel de Haën, methylene blue (MB) laboratory reagent from Paskem. Borosilicate glass slides of 2.5 cm × 7 cm and a thickness of 1 mm were obtained from Paksem.

2.2. Characterization

The nanostructure of the films was evaluated by a field emission gun scanning electron microscope (FEG-SEM) model Hitachi SU-70 FESEM. Its crystal nature and the lattice fringe spacing were analyzed by a transmission electron microscope (TEM) model TWIN 120 (TECNAI SPIRIT) equipped with a JEOL 100CF apparatus and coupled with selected area electron diffraction (SAED).

Both the thicknesses and the porosity of the films were measured by using a UV-NIR (193–1690 nm) M-2000DI spectroscopic ellipsometer from J. A. Woolllam. The measurements were conducted on the coated glass slide after soaking its bottom side with silicon oil and depositing it on the rigorous facet of a Silicon wafer. Ellipsometric ψ and Δ angle plots were recorded at 70° with the CompleteEASE software.

The crystalline phase of the coating was characterized with a D8 Discover X-ray diffractometer (Bruker), using a Cu emitter anode (Kα1 and Kα2 of wavelength 1.54056 and 1.5444 Å respectively) and a 1D LYNEXEYE XE-T detector. XRD measurements were performed on the coated glass substrates in grazing mode with an incidence angle fixed at 2°, and 0.05° steps.

The functional groups at the film's surface were analyzed by Fourier-transformed infrared (FTIR) in attenuated total reflection (ATR) mode with an incidence angle of 45°, and a 4 cm^{-1} resolution, using a Spectrum 400 model from PerkinElmer, equipped with an FR-DTGS detector (fast recovery Deuterated Triglycine Sulfate detector).

2.3. Synthesis of the wrinkled & porous ZnO photocatalyst

Firstly, an alcoholic solution of 0.1 M of Zn^{2+} was obtained by dissolving zinc acetate dihydrate (ZAD) in isopropanol (2-PrOH). Next, monoethanolamine (MEA) was added dropwise with a molar ratio of Zn^{2+}: MEA = 1. The sol was placed in a closed vessel and stirred for 1 h at T = 70 °C; below the boiling points of 2-PrOH (82.4 °C) and MEA (170 °C).

After aging for 24 h at room temperature (RT), ZnO sol was used to prepare multilayer films. Briefly, the glass slides were soaked in the sol and then withdrawn at 9 mm s^{-1} to an infrared chamber for pre-heat treatment at 150 °C. The same procedure was repeated 7 consecutive times to reach the desired thickness. Finally, the multilayers were then post-heated for 1 h at 450 °C to promote the crystallization of the ZnO network and remove the rest of the organic molecules [30,31]. The synthesis procedure of the wrinkled and porous ZnO thin films is detailed in our previous study [1].

2.4. Photo-Fenton and photocatalysis processes

- *Experimental Set-Up*

Fenton and photocatalysis experiments were conducted in batch Pyrex vessels of 50 mL, under UVA irradiation of λ = 365 nm. The UVA light source was placed at 5 cm from the reactors and an emitted illuminance of ~500 lux by a Testo 450 luxmeter of ±3 % precision from Testo, France. The vessels were filled with 45 ml of MB probe molecule (10 ppm) dissolved in deionized water (DI). The photocatalytic degradation of MB was carried out at room temperature (RT) for a maximum time of 8 h. The kinetic data was estimated by analyzing the absorbance curves, obtained by UV–vis spectroscopy. For the photo-Fenton-like experiments, H_2O_2, and Fe^{3+} were successively added in various molar ratios from 1:1 to 40000:1 to the MB solution under near-neutral pH (~7.5). For the photocatalysis experiments, ZnO thin films (11 cm^2) were immersed in the MB solution for 12 h in the dark to reach the adsorption equilibrium, before initiating the photocatalytic degradation process. As for the coupling experiments, the MB was added to the as-prepared ZnO films followed by the drop-wise addition of hydrogen peroxide and iron (III) reagent in a molar ratio of 130:1.

- *Kinetic Model*

The kinetics were estimated from the Langmuir–Hinshelwood kinetic model (Eq. (1)) [32]:

$$r = -\frac{dC}{dt} = \frac{Kr.K.C}{1 + K.C} \quad (1)$$

where r, C, K, K_r, and t represent the reaction rate, molecule concentration at time t, adsorption equilibrium constant, limiting rate constant of reaction at maximum coverage, and contact time respectively.

At small (mM) initial concentrations, ($K.C_0 \ll 1$), Eq. (2) is simplified to the apparent rate order (Eq. (2)) [32]:

$$r = -\frac{dC}{dt} = K_{app}.C \quad (2)$$

where K_{app}, is the apparent degradation rate. Simple integration of this equation for $C = C_0$ at $t = 0 = 0$ gives:

$$\ln\left(\frac{C_t}{C_0}\right) = -K_{app}.t \quad (3)$$

K_{app} is then obtained from the slope of the linear curve in the plot of $Ln\,(C_t/C_0)$ vs. t, where (C_t/C_0) is equal to (A_t/A_0) according to the Beer-Lambert law Eq. (4).

$$A = \varepsilon \times L \times C \quad (4)$$

A_0, A_t, C_0, C_t, ε & L refer respectively to the molecule light absorbance at t_0, molecule light absorbance at t, molecule concentration at t_0, molecule concentration at t, molar absorptivity, and length of the light path. The percentage of removal is obtained from (Eq. (5)) by estimating the concentration of MB during the experimental time.

$$\text{Efficiency} = \frac{C_0 - C_t}{C_0} \text{ x } 100 \quad (5)$$

3. Results and discussion

3.1. Characterization of the ZnO photocatalyst

The films' microstructure was investigated using SEM-FEG and HRTEM (Fig. 1a and b). The SEM-FEG micrographs reveal crack-free

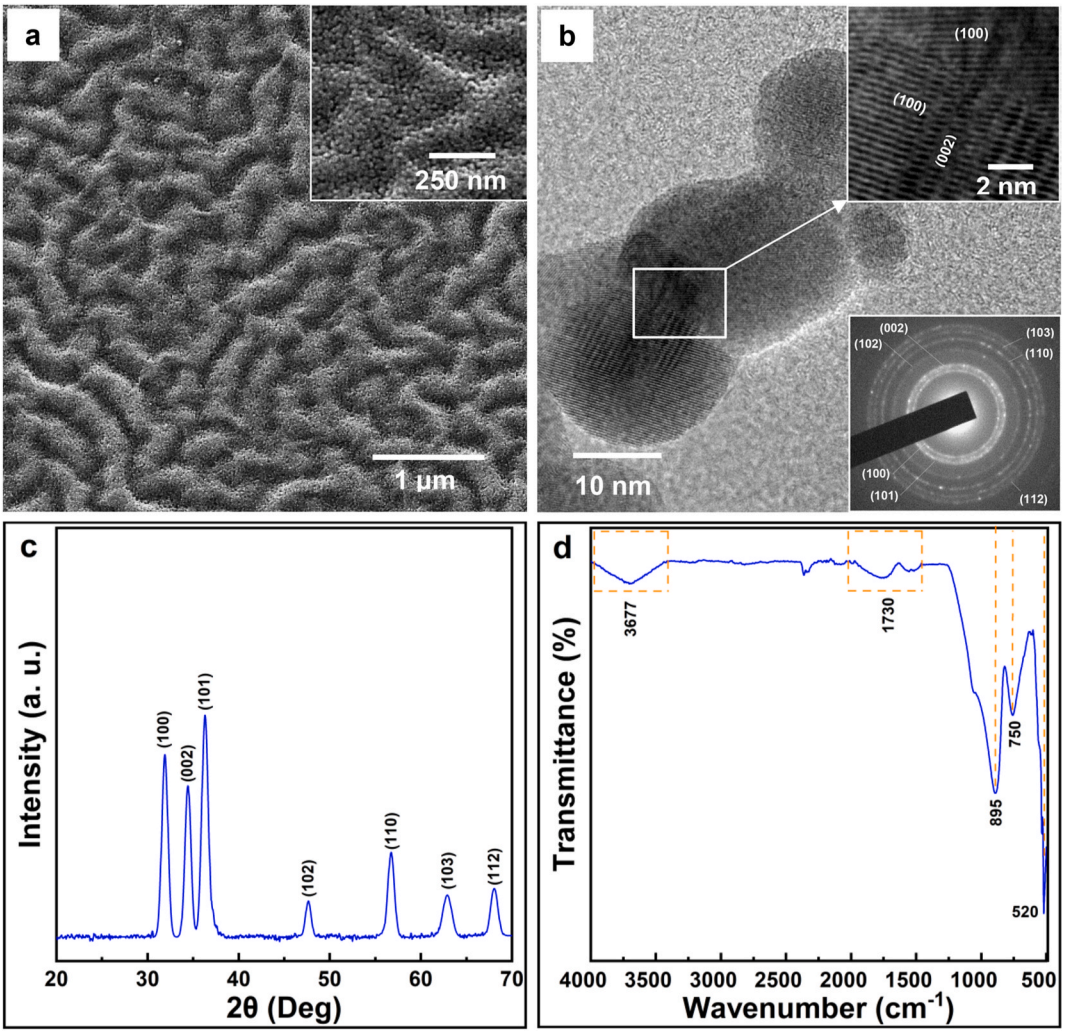

Fig. 1. **(a)** SEM-FEG micrographs of 7 layers' ZnO thin films post-heated treatment at 450 °C, Inset: Cross-sectional view of "a", **(b)** TEM image of the extracted grains from the film. Upper inset: HRTEM of identified grain boundaries. Bottom inset: SAEDpatternr, **(c)** X-ray diffraction pattern of "a", **(d)** ATR-FTIR spectrum of "a".

homogenous wrinkled and porous films. The ridges (protrusive areas) occupy a width between ~ 100 and 220 nm and stretch over a regular cleavage (hollow areas) between ~ 90 and 200 nm (valleys). The film's porosity was assessed by ellipsometry. A value of ~25% is achieved with a mean square error (MSE) of ~7.

High-resolution TEM images and SAED pattern (Fig. 1b) show well-defined grain boundaries and a polycrystalline structure, respectively. 7 distinctive concentric rings are identified with lattice spacing corresponding to the ZnO wurtzite crystalline structure (indexed in the bottom inset of Fig. 1b) [33–35]. Additionally, it can also be noticed the well-defined interface between two adjacent grains, as shown in the upper inset of Fig. 1b.

Grazing incidence X-ray diffraction was performed at an incidence angle of 2° (Fig. 1c). The XRD pattern of the multilayer thin films shows also 7 prominent peaks indexed with the (100), (002), (101), (102), (110), (103), and (112) crystallographic planes, representing a typical polycrystalline ZnO wurtzite structure. This agrees well with the SAED results [33–35]. The peaks' positions are indexed to the JCPDS No. 01-086-3978 with lattice constants: a = b = 3.248 Å and c = 5.202 Å.

The chemical composition of the coating was further supported by ATR-FTIR measurement (Fig. 1d). The vibrational behavior of the film's surface is characterized by 5 main functional groups located at 520, 750, 895, 1730, and 3677 cm^{-1}. The pronounced peak at ~520 cm^{-1} arises from the stretching vibration of Zn–O bonds [36]. The absorption bands at ~750 cm^{-1} and ~895 cm^{-1} are assigned to the stretching vibrations of Zn–O bonds [36–39] and the tetrahedral coordination of Zn within the hexagonal ZnO lattice [40], respectively. The broad absorption band at 4000–3500 cm^{-1} is attributed to the ZnO–H stretching, due to the hydroxylation of the film's surface by the atmospheric humidity [42]. The weak absorptions between ~1450 cm^{-1} and 2000 cm^{-1} are associated with C–H, C–H_2, C═C, and C═O stretching vibration bands probably due to the film's contamination by traces of organic molecules [43,44].

The optical bandgap energy (Eg) of the material was also calculated by using two different methods: i) plotting the first derivative of the absorbance (A) with respect to photon energy (E = $h\nu$), as a function of photon energy ((dA/dE) versus E), then founding Eg value at the first maximum on the lower energy side, and ii) plotting $(ah\nu)^2$ against $h\nu$ (a is the absorption coefficient), then finding the Eg value at the intersection between the extrapolation of the linear region of the curve with the abscissa (Fig. S1) [41]. Thus, a similar value of ~3.28 eV was obtained.

3.2. Optimization of H_2O_2 and Fe^{3+} concentrations

In Fenton-like oxidation, reaction kinetics are intimately dependent on the H_2O_2:Fe^{3+} ratio and irradiation light source. Thus, finding adequate proportions and quantities of reagents is crucial for reducing operating costs, and avoiding unwanted reactions [27]. For instance, a

surplus of H_2O_2 may scavenge the $^{\bullet}OH$ radicals generated via Rn. 2 [23]. In contrast, a low amount of H_2O_2 decreases the generation of $^{\bullet}OH$ and reduces the efficiency of the Fenton process. Furthermore, the application of light energy accelerates the radicals' generation and improves the process efficiency (Fig. S2).

The effect of $[H_2O_2]$ concentration on the degradation rate (K_{app}) of MB at 1 ppm $[Fe^{3+}]$ is shown in Fig. 2a. For ratios between 1:1 and 700:1, the rate constant follows a single linear trend. However, for higher ratios up to 40000:1, the MB degradation follows two distinct regimes, with slower kinetics between T_0 and 180 min, and faster kinetics between 180 and 420 min. At the first stage, $^{\bullet}OH$ radicals are scavenged by the excess of H_2O_2 to produce $HO_2^{\bullet}$ radicals with lower oxidation capability, hindering then the process kinetics [45,46]. As the experiment advances, hydrogen peroxide is partially consumed, disfavoring the scavenging reactions and leading to an increase in the $^{\bullet}OH$ free radicals. After 420 min, the rate constants become stable because all MB molecules are nearly degraded. The effect of H_2O_2 concentration on the degradation kinetics at 1 ppm $[Fe^{3+}]$ is summarized in Table S1.

Although the surplus of H_2O_2 improves drastically the kinetics degradation, its use at these concentrations is not recommended due to the increase of cost and risks in the overall process (associated with handling, transportation, and storage) [6].

The selection of the optimal $[H_2O_2]$:$[Fe^{3+}]$ (R) can be made by plotting d(K_{app})/dR vs R (between two consecutive values) as shown in Fig. 2b. The first derivative increases by ~1.8 times when R goes from 1:1 to 100:1, then reaches a maximum (~2.8) at R = 700:1 and finally decreases sharply to 0.04 for R = 40000:1. From this perspective, R = 700:1 yields the highest efficiency considering the given quantity of H_2O_2. Furthermore, this quantity of hydrogen peroxide is found to be equal to the stoichiometric amount ($[H_2O_2]$:[MB] = 52:1) required for the degradation of the 10 ppm MB [47].

In addition, the Fe^{3+} amount should be optimized to increase the degradation kinetics while keeping a low sludge production. To do so, the $[Fe^{3+}]$ range is varied from 1 ppm to 15 ppm at a fixed initial concentration of H_2O_2 ($[H_2O_2]$:[MB] = 52:1) (Fig. 3a).

When the catalyst concentration goes from 1 to 3 ppm, the degradation efficiency attains 22 % in 90 min of irradiation, corresponding to an increase in the rate constant by ~2.7 times. In this range, a linear degradation regime with no precipitate formation is observed (Fig. 3b). Nevertheless, while an increase in the iron(III) concentration to 15 ppm drastically improves the final removal of MB to 94 % in 90 min, the

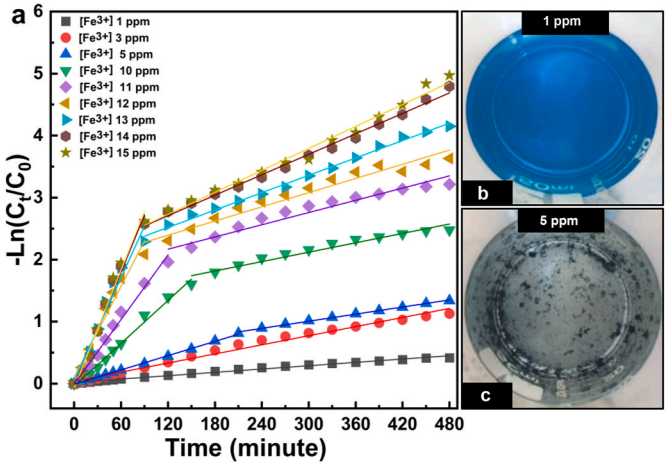

Fig. 3. **(a)** Degradation rates of 10 ppm MB under UVA (λ = 365 nm) at T = 25 °C, with different loads of Fe^{3+}, $\frac{[H_2O_2]}{[MB]}$ = 52. Top view of photo Fenton-like batch reactor with **(b)** 1 ppm, and **(c)** 5 ppm Fe^{3+} after 1 h of irradiation.

degradation kinetics follow two different regimes. The first one is attributed to the formation of additional hydroxyl radicals during the Fe^{3+}/Fe^{2+} regeneration, leading to a rapid increase in rate constants in the early stages of the process. However, the second one corresponds to the accumulation of iron sludge in the medium, resulting in a decrease in the degradation rate, and an appearance of an inflection point. For instance, at $[Fe^{3+}]$ = 5 ppm, the inflection appears at 210 min, showing the beginning of iron ions precipitation in the form of oxyhydroxide. The formation of this component is classified as a secondary source of pollution (Fig. 3c) [6]. This behavior is more pronounced at higher temperatures, where an increase from 25 to 30 °C shifts the inflection point from 210 to 60 min (Fig. S3) due to the higher frequency of collisions of species in the medium. In addition, augmenting the $[Fe^{3+}]$ from 5 to 15 ppm moves gradually the inflection point to 90 min, confirming the low regeneration of the Fe^{3+} catalyst at high concentrations [6].

The MB removal (%) after 90 min of irradiation (Table S2) is quite comparable with other reported homogeneous Fenton systems, working in acidic pH (3–4), and using chelating agents such as

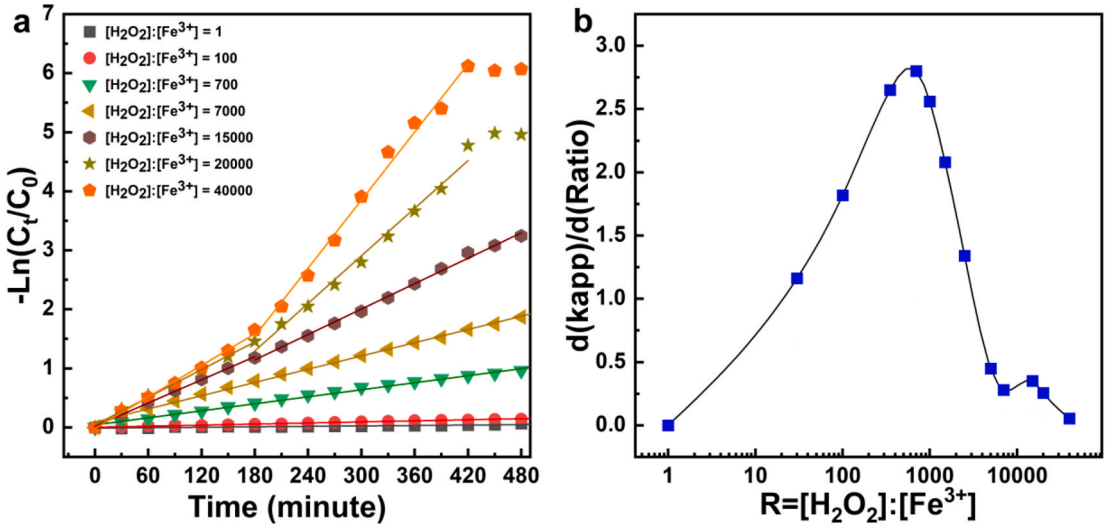

Fig. 2. **(a)** Degradation rates of 10 ppm methylene blue by different $\frac{[H_2O_2]}{[Fe^{3+}]}$ ratios with UVA light of λ = 365 nm, T = 25 °C. $[Fe^{3+}]$ was fixed at 1 ppm, **(b)** Fluctuation of d(K_{app})/dr vs r plots, representing the evolution of the kinetic constants K_{app} (min^{-1}) along the experimental progression of the $\frac{[H_2O_2]}{[Fe^{3+}]}$ ratio (R). (For interpretation of the references to colour in this figure legend, the reader is referred to the Web version of this article.)

ethylenediaminetetraacetic acid disodium (EDTA), and S,S-ethylenediamine-N,N-disuccinic acid trisodium salt (EDDS-Na) for reducing sludge formation [28,46,48–50]. However, all these approaches increase the operational cost, Total Organic Carbon (TOC) level in the water matrix, and can promote non-desirable reactions [51,52].

3.3. Coupling of the photocatalytic and photo-Fenton-like processes

The enhancement of reactions kinetics and the reduction of sludge formation can be realized by increasing the amount of ROS and the lifetime of electron - hole pairs. Accordingly, coupling the ZnO semiconductor with the Fe(III) and Fe(II) catalysts appears as an attractive approach. For instance, the photogenerated electrons in the ZnO conduction band reduce the Fe^{3+} ions instead of being recombined, leading to an increase in the oxidant radicals. To investigate the efficiency of the coupled processes, a [Fe^{3+}] concentration of 5 ppm was chosen at [H_2O_2]:[MB] = 52:1. This ratio corresponds to the beginning of the sludge formation.

Fig. 4 presents the kinetics degradation of MB for an irradiation time of 480 min, using three systems: i) wrinkled and porous ZnO thin films, ii) photo-Fenton-like, and iii) coupled ZnO with photo-Fenton-like. First, the ZnO thin films demonstrate a relatively low photocatalytic activity compared to the other systems. This is probably due to the low generation of ROS, promoted by the recombination of electron - hole pairs [53,54].

On the other side, the photo-Fenton-like process exhibits a higher degradation kinetic of 0.0038 min^{-1} during the first 210 min of irradiation, approximately twice that of the photocatalysis (0.002 min^{-1}). However, as the experiment proceeds, the kinetic of individual photo-Fenton-like starts declining to become close to that of the ZnO photocatalysts. This behavior is explained by the higher generation of radicals in the first part and the beginning of sludge formation in the second one (see section 2.2). On the contrary, the coupled processes exhibit a single degradation rate over the experimental time, with a K_{app} of 0.0049 $min^{-1} > K_{app}$ (photocatalysis) of 0.002 $min^{-1} + K_{app}$ (photo-Fenton-like) between 0.0022 and 0.0038 min^{-1}. This new system is able to enhance

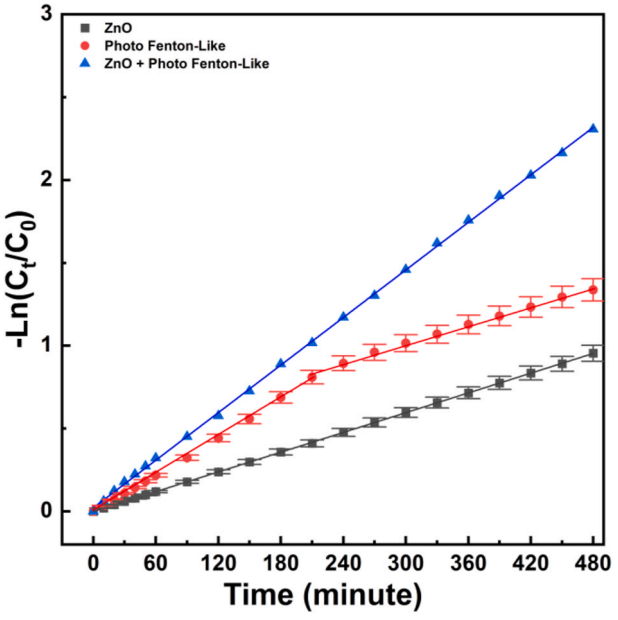

Fig. 4. Comparative degradation rate of 10 ppm methylene blue using ZnO photocatalyst, photo-Fenton-like, and the coupling of both under UVA light of λ = 365 nm, $\frac{[H_2O_2]}{[MB]} = 52$, and 5 ppm [$Fe^{3+}$] at T = 25 °C. (For interpretation of the references to colour in this figure legend, the reader is referred to the Web version of this article.)

the photocatalytic activity of ZnO and the performance of the photo-Fenton-like, simultaneously. When the zinc oxide is irradiated by a 365 nm light source, electron – hole pairs are generated and promote the oxidation/reduction of H_2O and O_2 molecules to produce $O_2^{\bullet-}$ and $^{\bullet}OH$ radicals. This phenomenon can accelerate the regeneration of Fe^{3+}/Fe^{2+} and reduces the electron – hole recombination (Fig. 5). The positioning of the ZnO conduction band (−0.31 V vs Normal Hydrogen Electrode (NHE)) enables the photogenerated electrons to reduce the Fe^{3+} ions to Fe^{2+} ($E_{0_{Fe(III)/Fe(II)}} = 0.77$ V vs NHE) and consequently limiting the $e^- - h^+$ recombination [55–57]. The iron(III) reduction is considered the rate-determining step because it is about 6000 times slower than iron(II) oxidation (Rn. 2) [6]. Furthermore, the free $^{\bullet}OH$ radicals produced by the reduction of the dissolved oxygen and the oxidation of water molecules contribute beside the H_2O_2 reagents to the regeneration of Fe^{3+} (Rn. 4) [6,58–62].

$$Fe^{2+} + HO^{\bullet} \rightarrow Fe^{3+} + OH^- \text{ (Fenton) (Rn. 4)}$$

Consequently, the generated ROS by the ZnO photocatalyst, and the Fe^{3+}/Fe^{2+} regeneration cycle participate altogether in the MB degradation (as seen in Fig. S4). Other radicals (e.g. $HO_2^{\bullet}$) generated via a classic photocatalytic system are also involved in the oxidation process and contribute to the mechanism in Fig. 5 (not shown for aesthetic purposes).

As a result, coupling the ZnO photocatalysis with the photo-Fenton like increases the rate constant of MB degradation to 0.0049 min^{-1} which bypasses the sum of the obtained kinetics from the individual processes (Fig. 4). Interestingly, some Fenton processes have reported high degradation kinetics in acidic pH (3–4) conditions and at temperatures between ~30 and 35 °C, or by using chelating agents. This novel design exhibits comparable performance to these approaches and other methods including adsorption, heterogeneous Fenton, and non-coupled ZnO photocatalysis (Table 1).

4. Conclusion

In this study, we propose a novel oxidation system to tackle organic pollutants in water at near-neutral pH and room temperature. Although the photocatalytic degradation of organic pollutants by using Fenton processes have been widely studied by numerous works, several limitations are still impeding their application: (i) the usage of H_2O_2 oxidant in relatively high amount is considered to be non-economical in additions to increasing the storage and transportation risks and adding extra costs; (ii) the accumulation of iron sludge, a component that is classified as a secondary source of pollution and requires further treatment; and (iii) the necessity of using extreme acidic conditions, (pH < 3). To tackle these constraints, we propose a novel system coupling wrinkled ZnO thin films of high surface area with an iron(III)/iron(II) homogeneous Fenton-like process.

The supported ZnO photocatalyst exhibited a crack-free homogenous wrinkled and porous films (25%), with regular ridges of ~100–220 nm stretching over ~ 90–200 nm cleavage, and was characterized with an optical bandgap energy of 3.28 eV. Therefore, the photocatalyst provides a relatively high surface area, to increase the contact between the ZnO thin films and MB/iron. Furthermore, by coupling the optimized Fenton system (low H_2O_2 concentration at neutral pH) with the ZnO photocatalyst, the MB removal reached 94% in 480 min, without any sludge formation. The iron catalyst plays the role of electron scavenger, therefore reducing the electron – hole recombination in the ZnO semiconductor. This system shows a higher degradation rate of 0.0049 min^{-1} than the two processes operating separately, due to the increase in free $^{\bullet}OH$ radicals and the rapid regeneration of Fe^{3+}/Fe^{2+}. Interestingly, this prevents the formation of ferrous sludge without using chelating agents, and allows therefore the apparition of a single degradation regime of MB. Moreover, compared to other works, this study presents several advantages including: i) a reduction of the process cost and risks (low

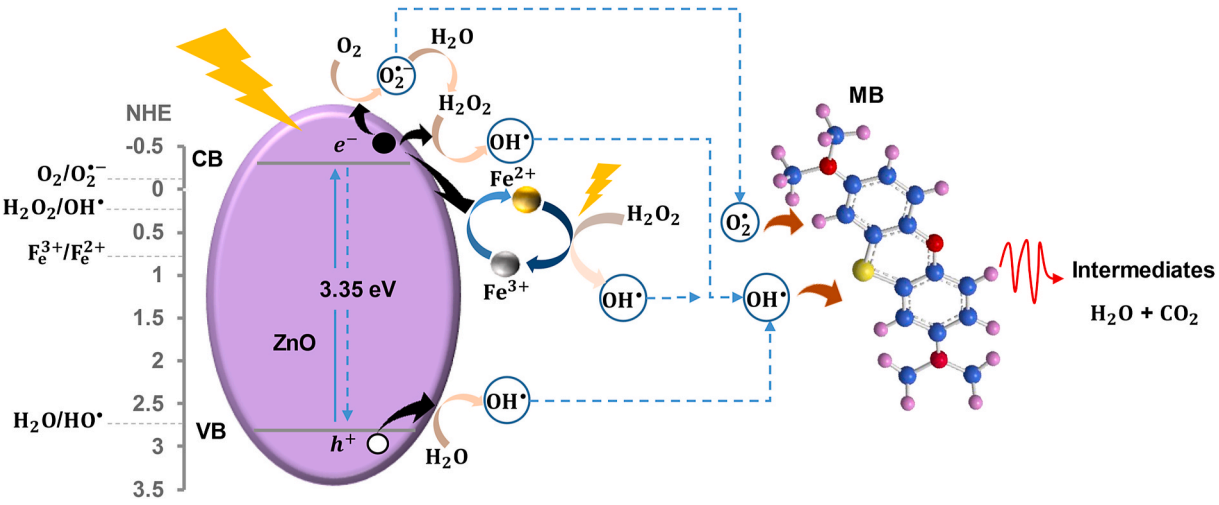

Fig. 5. Coupled system made of the ZnO photocatalyst and the photo-Fenton-like process.

Table 1
Working parameters and the kinetics of the as-synthesized ZnO photocatalyst, photo-Fenton-like, the coupled system, and other different methods such as adsorption, heterogeneous Fenton, and non-coupled ZnO photocatalysis.

Method	Working T (°C)	Working pH	[MB] (ppm)	[Fe^{3+}] (ppm)	[H_2O_2]: [Fe^{3+}] Molar ratio'	Light source	*Kapp* (min^{-1})	*MB removal* (%)
Fenton-like/Ferrocene [63]	30	4	10	N/A	N/A	N/A	N/A	100 in 90 min
Heterogeneous Fenton/$Fe_{3-x}Ti_xO_4$ [64]	RT	6.8	100	N/A	N/A	N/A	N/A	98 in 24 h
Adsorption/MCGO [65]	RT	N/A	30	N/A	N/A	N/A	N/A	96 in 14 h
ZnO nanorods [66]	25	N/A	3	N/A	N/A	Visible	~0.012	N/A
Dense ZnO film [67]	RT	N/A	~5	N/A	N/A	UVA	~0.0028	N/A
Wrinkled ZnO Photocatalyst (This study)	25	7.5	10	N/A	N/A	UVA (365 nm)	0.002	61 in 480 min
Photo-Fenton Like (This study)	25	7.5	10	5	130	UVA (365 nm)	0.0022–0.0038	73 in 480 min
Coupled system (This study)	25	7.5	10	5	130	UVA (365 nm)	0.0049	94 in 480 min

[H_2O_2] and [Fe^{3+}]), ii) a diminution of the equipment's corrosion (low [H_2O_2] and neutral pH), and iii) a decrease of the secondary pollution (no sludge formation).

Declaration of competing interest

The authors declare that they have no known competing financial interests or personal relationships that could have appeared to influence the work reported in this paper.

Acknowledgement

This work has been supported by the project: CLAIM, H2020-BG-2016–2017 [grant number 774586], "Cleaning Litter by Developing and Applying Innovative Methods in European seas". Mr. David Montero, Ms. Ferdaous Ben Romdhane, and Mr. Mohamed Selmane are gratefully acknowledged for conducting SEM-FEG, TEM, and XRD measurements at the Sorbonne University.

Appendix A. Supplementary data

Supplementary data to this article can be found online at https://doi.org/10.1016/j.ceramint.2024.02.243.

References

[1] E.A. Daher, B. Riachi, J. Chamoun, C. Laberty-Robert, W. Hamd, New approach for designing wrinkled and porous ZnO thin films for photocatalytic applications, Colloids Surf. A Physicochem. Eng. Asp. 658 (2023) 130628, https://doi.org/10.1016/j.colsurfa.2022.130628.
[2] N. Serpone, Photocatalysis, John Wiley & Sons, Inc., in: Kirk-Othmer Encyclopedia of Chemical Technology, John Wiley & Sons, Inc., Hoboken, NJ, USA, 2000, https://doi.org/10.1002/0471238961.1608152019051816.a01, 1608152019051816.a01
[3] K. Nakata, A. Fujishima, TiO2 photocatalysis: design and applications, J. Photochem. Photobiol. C Photochem. Rev. 13 (3) (Sep. 2012) 169–189, https://doi.org/10.1016/j.jphotochemrev.2012.06.001.
[4] M. Zhang, H. Dong, L. Zhao, D. Wang, D. Meng, A review on Fenton process for organic wastewater treatment based on optimization perspective, Sci. Total Environ. 670 (Jun. 2019) 110–121, https://doi.org/10.1016/j.scitotenv.2019.03.180.
[5] X. Jia, et al., g-C $_3$ N $_4$ -modified Zr-Fc MOFs as a novel photocatalysis-self-Fenton system toward the direct hydroxylation of benzene to phenol, RSC Adv. 13 (28) (2023) 19140–19148, https://doi.org/10.1039/D3RA03055E.
[6] W.S. Hamd, J. Dutta, Heterogeneous photo-Fenton reaction and its enhancement upon addition of chelating agents, in: Nanomaterials for the Detection and Removal of Wastewater Pollutants, Elsevier, 2020, pp. 303–330, https://doi.org/10.1016/B978-0-12-818489-9.00011-6.
[7] S. Ghosh, et al., Conducting polymer nanostructures for photocatalysis under visible light, Nat. Mater. 14 (5) (May 2015) 505–511, https://doi.org/10.1038/nmat4220.
[8] L. Zeng, X. Guo, C. He, C. Duan, Metal–organic frameworks: versatile materials for heterogeneous photocatalysis, ACS Catal. 6 (11) (Nov. 2016) 7935–7947, https://doi.org/10.1021/acscatal.6b02228.
[9] D.B. Miklos, C. Remy, M. Jekel, K.G. Linden, J.E. Drewes, U. Hübner, Evaluation of advanced oxidation processes for water and wastewater treatment – a critical review, Water Res. 139 (Aug. 2018) 118–131, https://doi.org/10.1016/j.watres.2018.03.042.

[10] J. Lin, H. Hu, N. Gao, J. Ye, Y. Chen, H. Ou, Fabrication of GO@MIL-101(Fe) for enhanced visible-light photocatalysis degradation of organophosphorus contaminant, J. Water Process Eng. 33 (Feb. 2020) 101010, https://doi.org/10.1016/j.jwpe.2019.101010.
[11] R.X. De S. Furtado, C.A. Sabatini, M. Zaiat, E.B. Azevedo, Perfluorooctane sulfonic acid (PFOS) degradation by optimized heterogeneous photocatalysis (TiO2/UV) using the response surface methodology (RSM), J. Water Process Eng. 41 (Jun. 2021) 101986, https://doi.org/10.1016/j.jwpe.2021.101986.
[12] I.Y. Habib, et al., Effect of Cr doping in CeO2 nanostructures on photocatalysis and H2O2 assisted methylene blue dye degradation, Catal. Today 375 (Sep. 2021) 506–513, https://doi.org/10.1016/j.cattod.2020.04.008.
[13] O. Baaloudj, I. Assadi, N. Nasrallah, A. El Jery, L. Khezami, A.A. Assadi, Simultaneous removal of antibiotics and inactivation of antibiotic-resistant bacteria by photocatalysis: a review, J. Water Process Eng. 42 (Aug. 2021) 102089, https://doi.org/10.1016/j.jwpe.2021.102089.
[14] K.M. Lee, C.W. Lai, K.S. Ngai, J.C. Juan, Recent developments of zinc oxide based photocatalyst in water treatment technology: a review, Water Res. 88 (Jan. 2016) 428–448, https://doi.org/10.1016/j.watres.2015.09.045.
[15] A. Uheida, H.G. Mejía, M. Abdel-Rehim, W. Hamd, J. Dutta, Visible light photocatalytic degradation of polypropylene microplastics in a continuous water flow system, J. Hazard Mater. 406 (Mar. 2021) 124299, https://doi.org/10.1016/j.jhazmat.2020.124299.
[16] S. Dobretsov, P. Sathe, T. Bora, M. Barry, M.T.Z. Myint, M.A. Abri, Toxicity of different zinc oxide nanomaterials at 3 trophic levels: implications for development of low-toxicity antifouling agents, Environ. Toxicol. Chem. 39 (7) (Jul. 2020) 1343–1354, https://doi.org/10.1002/etc.4720.
[17] Y. Li, et al., Green synthesis of red mud based ZnO Fe2O3 composite used for photo-Fenton reaction under visible light, J. Clean. Prod. 207 (Jan. 2019) 717–727, https://doi.org/10.1016/j.jclepro.2018.10.051.
[18] I. Ahmad, et al., Recent progress in rare earth oxides and carbonaceous materials modified ZnO heterogeneous photocatalysts for environmental and energy applications, J. Environ. Chem. Eng. 10 (3) (Jun. 2022) 107762, https://doi.org/10.1016/j.jece.2022.107762.
[19] C. Dong, et al., Self-cycled photo-Fenton-like system based on an artificial leaf with a solar-to-H2O2 conversion efficiency of 1.46%, Nat. Commun. 13 (1) (Aug. 2022) 4982, https://doi.org/10.1038/s41467-022-32410-0.
[20] Ö. Görmez, F. Görmez, B. Gözmen, Comparison of the heterogeneous GO-FePO4/electro-Fenton against the homogeneous Fe(II) ion and Fe(III)-oxalate complex/electro-Fenton for the degradation of metronidazole, J. Water Process Eng. 43 (Oct. 2021) 102265, https://doi.org/10.1016/j.jwpe.2021.102265.
[21] F. Zhao, Y. Yang, S. Ji, R. Yu, X. Li, Z. Zhou, Photocatalysis-Fenton mechanism of rGO-enhanced Fe-doped carbon nitride with boosted degradation performance towards rhodamine B, J. Water Process Eng. 55 (Oct. 2023) 104080, https://doi.org/10.1016/j.jwpe.2023.104080.
[22] Y. Cardona, A. Węgrzyn, P. Miśkowiec, S.A. Korili, A. Gil, Heterogeneous Fenton- and photo-Fenton-like catalytic degradation of emerging pollutants using Fe2O3/TiO2/pillared clays synthesized from aluminum industrial wastes, J. Water Process Eng. 52 (Apr. 2023) 103494, https://doi.org/10.1016/j.jwpe.2023.103494.
[23] S. Ziembowicz, M. Kida, Limitations and future directions of application of the Fenton-like process in micropollutants degradation in water and wastewater treatment: a critical review, Chemosphere 296 (Jun. 2022) 134041, https://doi.org/10.1016/j.chemosphere.2022.134041.
[24] M. Xia, M. Long, Y. Yang, C. Chen, W. Cai, B. Zhou, A highly active bimetallic oxides catalyst supported on Al-containing MCM-41 for Fenton oxidation of phenol solution, Appl. Catal. B Environ. 110 (Nov. 2011) 118–125, https://doi.org/10.1016/j.apcatb.2011.08.033.
[25] M. Zhang, Q. Yao, W. Guan, C. Lu, J.-M. Lin, Layered double hydroxide-supported carbon dots as an efficient heterogeneous fenton-like catalyst for generation of hydroxyl radicals, J. Phys. Chem. C 118 (19) (May 2014) 10441–10447, https://doi.org/10.1021/jp5012268.
[26] Y. Liu, W. Jin, Y. Zhao, G. Zhang, W. Zhang, Enhanced catalytic degradation of methylene blue by α-Fe2O3/graphene oxide via heterogeneous photo-Fenton reactions, Appl. Catal. B Environ. 206 (Jun. 2017) 642–652, https://doi.org/10.1016/j.apcatb.2017.01.075.
[27] C. Dong, M. Xing, J. Zhang, Recent progress of photocatalytic fenton-like process for environmental remediation, Front. Environ. Chem. 1 (Sep. 2020) 8, https://doi.org/10.3389/fenvc.2020.00008.
[28] C. Sun, C. Chen, W. Ma, J. Zhao, Photodegradation of organic pollutants catalyzed by iron species under visible light irradiation, Phys. Chem. Chem. Phys. 13 (6) (2011) 1957–1969, https://doi.org/10.1039/C0CP01203C.
[29] P. Bansal, A. Verma, C. Mehta, J. Singla, A.P. Toor, Assessment of integrated binary process by coupling photocatalysis and photo-Fenton for the removal of cephalexin from aqueous solution, J. Mater. Sci. 53 (10) (May 2018) 7326–7343, https://doi.org/10.1007/s10853-018-2094-x.
[30] W. Hamd, A. Boulle, E. Thune, R. Guinebretiere, A new way to prepare tin oxide precursor polymeric gels, J. Sol. Gel Sci. Technol. 55 (1) (Jul. 2010) 15–18, https://doi.org/10.1007/s10971-010-2206-9.
[31] M. Dumoulin, W. Hamd, E. Thune, C. Rochas, R. Guinebretiere, *In situ* time-resolved small-angle X-ray scattering observation of the fractal aggregation process in tin alkoxide polymeric solution, J. Appl. Crystallogr. 49 (2) (Apr. 2016) 366–374, https://doi.org/10.1107/S1600576716000297.
[32] K.V. Kumar, K. Porkodi, F. Rocha, Langmuir–Hinshelwood kinetics – a theoretical study, Catal. Commun. 9 (1) (Jan. 2008) 82–84, https://doi.org/10.1016/j.catcom.2007.05.019.
[33] Y. Liu, W. Gao, Growth process, crystal size and alignment of ZnO nanorods synthesized under neutral and acid conditions, J. Alloys Compd. 629 (Apr. 2015) 84–91, https://doi.org/10.1016/j.jallcom.2014.12.139.
[34] L.N. Demianets, D.V. Kostomarov, Mechanism of zinc oxide single crystal growth under hydrothermal conditions, Ann. Chim. Sci. Matér. 26 (1) (2001) 193–198.
[35] T. Bora, P. Sathe, K. Laxman, S. Dobretsov, J. Dutta, Defect engineered visible light active ZnO nanorods for photocatalytic treatment of water, Catal. Today 284 (Apr. 2017) 11–18, https://doi.org/10.1016/j.cattod.2016.09.014.
[36] M. S, H. N, P.P. V, In vitro biocompatibility and antimicrobial activities of zinc oxide nanoparticles (ZnO NPs) prepared by chemical and green synthetic route— a comparative study, BioNanoScience 10 (1) (Mar. 2020) 112–121, https://doi.org/10.1007/s12668-019-00698-w.
[37] T.L. Valerio, G.A.R. Maia, L.F. Gonçalves, A. Viomar, E. do P. Banczek, P.R. P. Rodrigues, Study of the Nb2O5 insertion in ZnO to dye-sensitized solar cells, Mater. Res. 22 (suppl 1) (2019) e20180864, https://doi.org/10.1590/1980-5373-mr-2018-0864.
[38] J. Singh, S. Kaur, G. Kaur, S. Basu, M. Rawat, Biogenic ZnO nanoparticles: a study of blueshift of optical band gap and photocatalytic degradation of reactive yellow 186 dye under direct sunlight, Green Process. Synth. 8 (1) (Jan. 2019) 272–280, https://doi.org/10.1515/gps-2018-0084.
[39] S. Bai, J. Hu, D. Li, R. Luo, A. Chen, C.C. Liu, Quantum-sized ZnO nanoparticles: synthesis, characterization and sensing properties for NO2, J. Mater. Chem. 21 (33) (2011) 12288, https://doi.org/10.1039/c1jm11302j.
[40] M.L. da Silva-Neto, et al., UV random laser emission from flexible ZnO-Ag-enriched electrospun cellulose acetate fiber matrix, Sci. Rep. 9 (1) (Aug. 2019) 11765, https://doi.org/10.1038/s41598-019-48056-w.
[41] E.A. Daher, C. Boissière, C.L. Robert, W. Hamd, Investigating the impact of chemical structures on the photocatalytic degradation rates over ZnO nanorods: an oxidative pathways perspective, Catal. Commun. 185 (Dec. 2023) 106807, https://doi.org/10.1016/j.catcom.2023.106807.
[42] Inamuddin, N. Shakeel, M. Imran Ahamed, S. Kanchi, H. Abbas Kashmery, Green synthesis of ZnO nanoparticles decorated on polyindole functionalized-MCNTs and used as anode material for enzymatic biofuel cell applications, Sci. Rep. 10 (1) (Mar. 2020) 5052, https://doi.org/10.1038/s41598-020-61831-4.
[43] S. Pramanik, et al., Role of oxygen vacancies on the green photoluminescence of microwave-assisted grown ZnO nanorods, J. Alloys Compd. 849 (Dec. 2020) 156684, https://doi.org/10.1016/j.jallcom.2020.156684.
[44] X. Zhang, H. Shi, E. Liu, X. Hu, K. Zhang, J. Fan, Preparation of polycrystalline ZnO nanoparticles loaded onto graphene oxide and their antibacterial properties, Mater. Today Commun. 28 (Sep. 2021) 102531, https://doi.org/10.1016/j.mtcomm.2021.102531.
[45] N.R. Mohanty, I.W. Wei, Oxidation of 2,4-dinitrotoluene using fenton's reagent: reaction mechanisms and their practical applications, Hazard Waste Hazard. Mater. 10 (2) (Jan. 1993) 171–183, https://doi.org/10.1089/hwm.1993.10.171.
[46] K. Dutta, S. Mukhopadhyay, S. Bhattacharjee, B. Chaudhuri, Chemical oxidation of methylene blue using a Fenton-like reaction, J. Hazard Mater. 84 (1) (Jun. 2001) 57–71, https://doi.org/10.1016/S0304-3894(01)00202-3.
[47] I.A. Salem, M.S. El-Maazawi, Kinetics and mechanism of color removal of methylene blue with hydrogen peroxide catalyzed by some supported alumina surfaces, Chemosphere 41 (8) (Oct. 2000) 1173–1180, https://doi.org/10.1016/S0045-6535(00)00009-6.
[48] W. Huang, M. Brigante, F. Wu, K. Hanna, G. Mailhot, Development of a new homogenous photo-Fenton process using Fe(III)-EDDS complexes, J. Photochem. Photobiol. Chem. 239 (Jul. 2012) 17–23, https://doi.org/10.1016/j.jphotochem.2012.04.018.
[49] Q. Wang, S. Tian, P. Ning, Ferrocene-Catalyzed heterogeneous fenton-like degradation of methylene blue: influence of initial solution pH, Ind. Eng. Chem. Res. 53 (15) (Apr. 2014) 6334–6340, https://doi.org/10.1021/ie500115j.
[50] Y. Hu, et al., EDTA-Fe(III) Fenton-like oxidation for the degradation of malachite green, J. Environ. Manag. 226 (Nov. 2018) 256–263, https://doi.org/10.1016/j.jenvman.2018.08.029.
[51] T.T.T. Tran, K. Kannoorpatti, A. Padovan, S. Thennadil, Effect of pH regulation by sulfate-reducing bacteria on corrosion behaviour of duplex stainless steel 2205 in acidic artificial seawater, R. Soc. Open Sci. 8 (1) (Jan. 2021) 200639, https://doi.org/10.1098/rsos.200639.
[52] U.J. Ahile, R.A. Wuana, A.U. Itodo, R. Sha'Ato, R.F. Dantas, A review on the use of chelating agents as an alternative to promote photo-Fenton at neutral pH: current trends, knowledge gap and future studies, Sci. Total Environ. 710 (Mar. 2020) 134872, https://doi.org/10.1016/j.scitotenv.2019.134872.
[53] A.G. Vega-Poot, et al., Mechanisms of electron transport and recombination in ZnO nanostructures for dye-sensitized solar cells, ChemPhysChem 15 (6) (Apr. 2014) 1088–1097, https://doi.org/10.1002/cphc.201301068.
[54] B. Abebe, E.A. Zereffa, A. Tadesse, H.C.A. Murthy, A review on enhancing the antibacterial activity of ZnO: mechanisms and microscopic investigation, Nanoscale Res. Lett. 15 (1) (Dec. 2020) 190, https://doi.org/10.1186/s11671-020-03418-6.
[55] G. Xi, S. Ouyang, J. Ye, General synthesis of hybrid TiO2 mesoporous 'French fries' toward improved photocatalytic conversion of CO2 into hydrocarbon fuel: a case of TiO2/ZnO, Chem. Eur J. 17 (33) (Aug. 2011) 9057–9061, https://doi.org/10.1002/chem.201100580.
[56] A. Wu, et al., ZnO-dotted porous ZnS cluster microspheres for high efficient, Pt-free photocatalytic hydrogen evolution, Sci. Rep. 5 (1) (Mar. 2015) 8858, https://doi.org/10.1038/srep08858.
[57] C. Ding, et al., Fluorescent nanoscale covalent organic frameworks with the theoretically matched redox potential of Fe^{3+}/Fe^{2+} for monitoring of adenosine-

5′-triphosphate in cells, ACS Appl. Nano Mater. 4 (12) (Dec. 2021) 13132–13139, https://doi.org/10.1021/acsanm.1c02681.
[58] W. He, H.-K. Kim, W.G. Wamer, D. Melka, J.H. Callahan, J.-J. Yin, Photogenerated charge carriers and reactive oxygen species in ZnO/Au hybrid nanostructures with enhanced photocatalytic and antibacterial activity, J. Am. Chem. Soc. 136 (2) (Jan. 2014) 750–757, https://doi.org/10.1021/ja410800y.
[59] X. Zeng, Y. Liu, X. Hu, X. Zhang, Photoredox catalysis over semiconductors for light-driven hydrogen peroxide production, Green Chem. 23 (4) (2021) 1466–1494, https://doi.org/10.1039/D0GC04236F.
[60] X. Zhang, et al., Electrochemical oxygen reduction to hydrogen peroxide at practical rates in strong acidic media, Nat. Commun. 13 (1) (May 2022) 2880, https://doi.org/10.1038/s41467-022-30337-0.
[61] J. Li, et al., Vanadium dioxide nanocoating induces tumor cell death through mitochondrial electron transport chain interruption, Glob. Chall. 3 (3) (Mar. 2019) 1800058, https://doi.org/10.1002/gch2.201800058.
[62] H.D. Martin, et al., Chemistry of carotenoid oxidation and free radical reactions, Pure Appl. Chem. 71 (12) (Jan. 1999) 2253–2262, https://doi.org/10.1351/pac199971122253.
[63] Q. Wang, S. Tian, P. Ning, Degradation mechanism of methylene blue in a heterogeneous fenton-like reaction catalyzed by ferrocene, Ind. Eng. Chem. Res. 53 (2) (Jan. 2014) 643–649, https://doi.org/10.1021/ie403402q.
[64] S. Yang, et al., Decolorization of methylene blue by heterogeneous Fenton reaction using Fe3−xTixO4 (0≤x≤0.78) at neutral pH values, Appl. Catal. B Environ. 89 (3–4) (Jul. 2009) 527–535, https://doi.org/10.1016/j.apcatb.2009.01.012.
[65] H. Shi, W. Li, L. Zhong, C. Xu, Methylene blue adsorption from aqueous solution by magnetic cellulose/graphene oxide composite: equilibrium, kinetics, and thermodynamics, Ind. Eng. Chem. Res. 53 (3) (Jan. 2014) 1108–1118, https://doi.org/10.1021/ie4027154.
[66] S. Baruah, M.A. Mahmood, M.T.Z. Myint, T. Bora, J. Dutta, Enhanced visible light photocatalysis through fast crystallization of zinc oxide nanorods, Beilstein J. Nanotechnol. 1 (Nov. 2010) 14–20, https://doi.org/10.3762/bjnano.1.3.
[67] A.H. Navidpour, et al., Plasma-sprayed photocatalytic zinc oxide coatings, J. Therm. Spray Technol. 26 (4) (Apr. 2017) 717–727, https://doi.org/10.1007/s11666-017-0541-x.